

Full length Article

Total exhumation across the Beichuan fault in the Longmen Shan (eastern Tibetan plateau, China): Constraints from petrology and thermobarometry



Laura Airaghi^{a,*}, Julia de Sigoyer^a, Pierre Lanari^b, Stéphane Guillot^a, Olivier Vidal^a, Patrick Monié^c, Benjamin Sautter^d, Xibin Tan^e

^a Université Grenoble Alpes, ISTerre, F-38058 Grenoble, France

^b Institute of Geological Sciences, University of Bern, Baltzstrasse 1 + 3, CH-3012 Bern, Switzerland

^c Géosciences Montpellier, Université de Montpellier, CNRS, 34095 Montpellier, France

^d ENS, Laboratoire de Géologie, 24 rue Lhomond, 75005 Paris, France

^e Key Laboratory of Active Fault and Volcano, Institute of Geology, China Earthquake Administration, Beijing 100029, China

ARTICLE INFO

Keywords:

Longmen Shan
Tibetan plateau
Beichuan fault
total exhumation of the Pengguan massif
Fault offset
Greenschist metamorphism
Thermobarometry
⁴⁰Ar/³⁹Ar dating
Lower Cretaceous

ABSTRACT

The deep structure and deformation mechanisms of the Longmen Shan thrust belt (Sichuan, China), at the eastern border of the Tibetan plateau, were largely debated after the devastating Mw 7.9 Wenchuan earthquake (2008). Recent geophysical studies and field investigations have been focused on the active motion of the major Beichuan fault, which ruptured during the earthquake. However, the total exhumation across the fault still remains unclear. In the hanging wall of the Beichuan fault, the South China block is exhumed in the Pengguan massif. Close to the Beichuan fault, the rocks of the Pengguan massif underwent greenschist facies metamorphism associated with brittle-ductile deformation. No metamorphism is observed in the footwall of the fault. In this study, we characterize and date the metamorphic history recorded in the hanging wall of the Beichuan fault in order to constrain the depth and timing of exhumation of the rocks of the Pengguan massif along the fault. A high-resolution petrological approach involving chemical analyses and X-ray maps was used to analyze the micrometric metamorphic minerals. The P-T conditions of the greenschist facies metamorphic event were estimated by an inverse multi-equilibrium thermodynamic approach. The results, 280 ± 30 °C and 7 ± 1 kbar, suggest that the rocks of the Pengguan massif were exhumed from ca. 20 km depth. Our results underline the importance of the thrusting component in the long-term behavior of the Beichuan fault and provide a minimal depth at which the fault is rooted. In situ laser ablation ⁴⁰Ar/³⁹Ar dating of metamorphic white mica revealed that the greenschist overprint occurred at 135–140 Ma.

The Pengguan massif was therefore partially thrust along the Beichuan fault during the Lower Cretaceous, long before the Eocene-Miocene exhumation phase which is well-constrained by low-temperature thermochronology. Our results provide the first independent depth information for the exhumation history of the Pengguan massif and reveal a previously undocumented Lower Cretaceous tectonic event that marks the onset of the thick-skinned deformation in the external domain of the Longmen Shan (East of the Wenchuan Fault).

1. Introduction

On 12 May 2008, the Mw 7.9 Wenchuan earthquake affected the Longmen Shan (LMS) thrust belt at the eastern border of the Tibetan Plateau (Fig. 1). The underestimation of the seismic hazard before the 2008 seismic event was due to the apparent tectonic quiescence of the Longmen Shan. Recent GPS surveys show convergence rates of < 3 mm/y between the Tibetan plateau and the South China block (King et al., 1997; Shen et al., 2005; Zhang et al., 2011) despite a topographic step higher than 5000 m observed across the belt (Godard et al., 2009).

This devastating event threw into question previous ideas about the deformation mechanisms and the deep structure of the Longmen Shan thrust belt. Receiver function profiles show a sharp deepening of the Moho discontinuity across the belt, from ca. 40 km beneath the Sichuan basin to the East, to more than 60 km beneath the Songpan-Ganze (SPG) block to the West (Robert et al., 2010a,b; Zhang et al., 2009, 2010) (Fig. 2b). A crustal shortening model (Hubbard and Shaw, 2009; Hubbard et al., 2010) proposed to explain the Cenozoic deformation observed within the Longmen Shan cannot account for the total crustal thickness observed beneath the Songpan-Ganze block. The discrepancy

* Corresponding author.

E-mail address: laura.airaghi@univ-grenoble-alpes.fr (L. Airaghi).

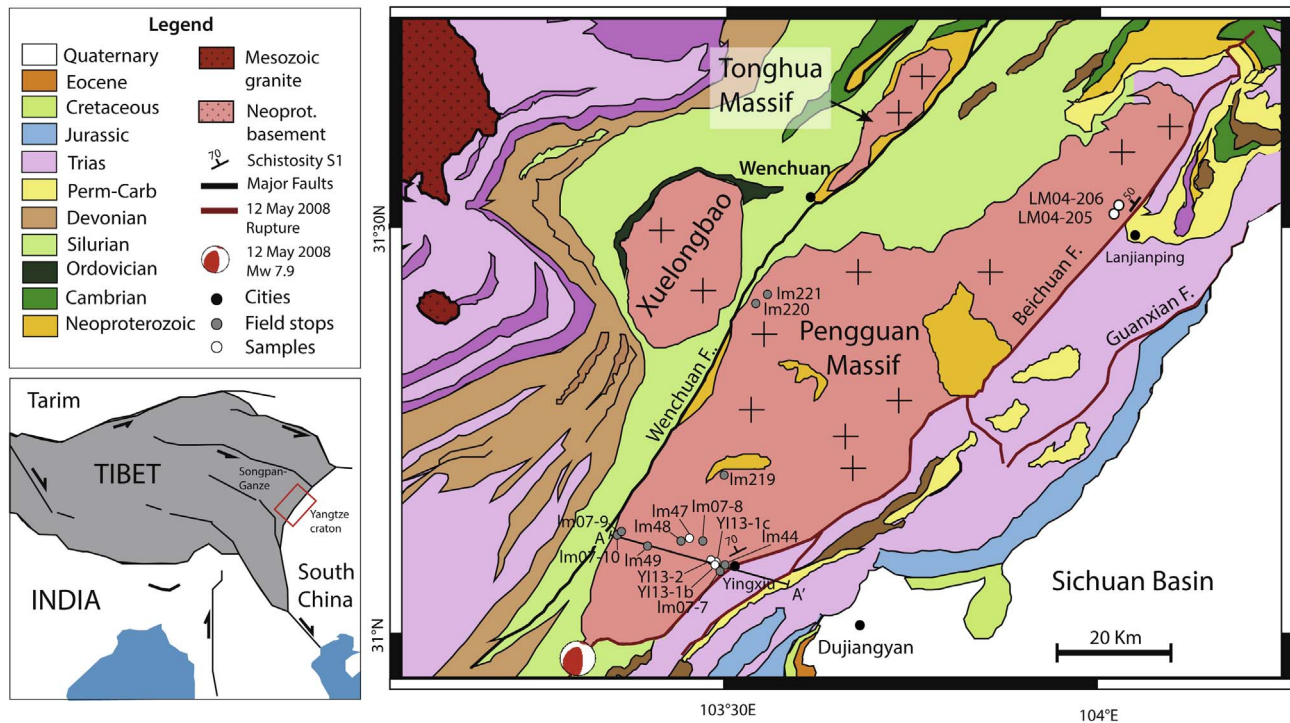


Fig. 1. Simplified geological map of the Longmen Shan thrust belt showing the Neoproterozoic basement of South China craton (Pengguan Massif) outcropping through the Paleozoic-Mesozoic sedimentary cover. The segments of the major Beichuan and Guanxian faults which ruptured during the 2008 Wenchuan earthquake are indicated in red. Location of samples is shown with white dots. Grey dots are field localities described in Section 2.1. The black line indicates the location of the profile for the cross sections of Fig. 2. (For interpretation of the references to colour in this figure legend, the reader is referred to the web version of this article.)

between the amount of shortening along the thrust belt and the total crustal thickness requires a more precise knowledge of the fault system architecture. Geophysical studies suggest the existence of a basal detachment extending westwards in the Songpan-Ganze block at a depth of 15–25 km (Wang et al., 2009, 2013; Robert et al., 2010a; Liu et al., 2014; Qi et al., 2011; Shen et al., 2009; Jia et al., 2010; Zhao et al., 2012) where the major faults of the Longmen Shan may be rooted (Fig. 2b). However whether a decollement exists or not at such depth is far from settled.

Three northwest dipping fault zones extend parallel to the trend of the Longmen Shan belt: the Wenchuan-Maowen fault (WMF) that lies in the Wenchuan Shear Zone (WSZ), in the Northwest of the belt, the Beichuan fault (BF) in the middle and the Guanxian fault (GF) in the eastern part of the LMS (Fig. 1). The WSZ separates a more western internal domain of the belt, metamorphosed to medium grades from a more eastern external domain metamorphosed to lower grades (Airaghi et al., 2017; Yan et al., 2008; Worley and Wilson, 1996; Dirks et al., 1994). The Moho step is located below the WMF fault zone while the topographic step is marked by the Beichuan fault (Fig. 2b). In the hanging wall of the BF, and bounded to the West by the WSZ, the South China block is exhumed in the Pengguan crystalline massif (Figs. 1 and 2a). Close to the fault zone the Pengguan massif is affected by a greenschist facies metamorphic event. On the contrary, no metamorphic history is recorded in the Paleozoic to Mesozoic sedimentary cover of the footwall of the Beichuan fault. This sharp lithological and metamorphic contrast observed across the Beichuan fault shows that it plays a major role in the exhumation of the basement from depth, as already suggested by the thermochronological study of Godard et al. (2009) and geomorphological analyses of Kirby et al. (2003) and Kirby and Ouimet (2011). Nevertheless the long-term exhumation occurring along the BF still remains unclear: from which depth was the basement exhumed? When did exhumation occur?

Here we have characterized the metamorphic conditions of the Pengguan crystalline massif for the first time in order to constrain the exhumation depth, and to discuss the timing of the exhumation. A

detailed high-resolution petrological study was coupled with *in-situ* $^{40}\text{Ar}/^{39}\text{Ar}$ dating on metamorphic white mica. We therefore provide an independent set of data for the timing and total exhumation recorded in the hanging wall of the Beichuan fault, a key point for constraining the long-term thrusting and thickening process in the Longmen Shan as well as the onset of the activity of the Beichuan fault.

2. Geological setting

The Longmen Shan thrust belt is located at the eastern border of the Tibetan plateau at the boundary between the South China block to the East and the Songpan-Ganze block to the West (Fig. 1). The belt records a multi-phased deformation history (Airaghi et al., 2017; Burchfiel et al., 1995; Worley and Wilson, 1996): the most recent deformation event occurred during the Cenozoic as a consequence of the India-Asia collision and the uplift of the Tibetan plateau (Yong et al., 2006). Thermochronological data show an increase in the exhumation rate across the belt since 30 Ma (Wang et al., 2012; Tan et al., 2014) associated with 36 km of shortening in the frontal part of the belt (Hubbard and Shaw, 2009). The Cenozoic reactivation overprinted a previous Mesozoic compressional event responsible for the structuration of the LMS, enhanced by the closure of the Paleotethys and the subsequent collision among the North China, the South China and the Qiangtang blocks since the Middle Triassic (Roger et al., 2010; de Sigoyer et al., 2014).

Field investigations show that the Sichuan basin is composed of a thin continental crust covered by a series of proximal sediments (Burchfiel et al., 1995; Chen and Wilson, 1995). Seismic profiles document the existence of Paleozoic extensional basins in the Sichuan basin (Jia et al., 2006). These observations suggest that the South China basement was composed of tilted blocks when the Early Mesozoic compressional event began. The active Beichuan and Wenchuan faults may then represent inherited structures reactivated during basin inversion (Burchfiel et al., 1995).

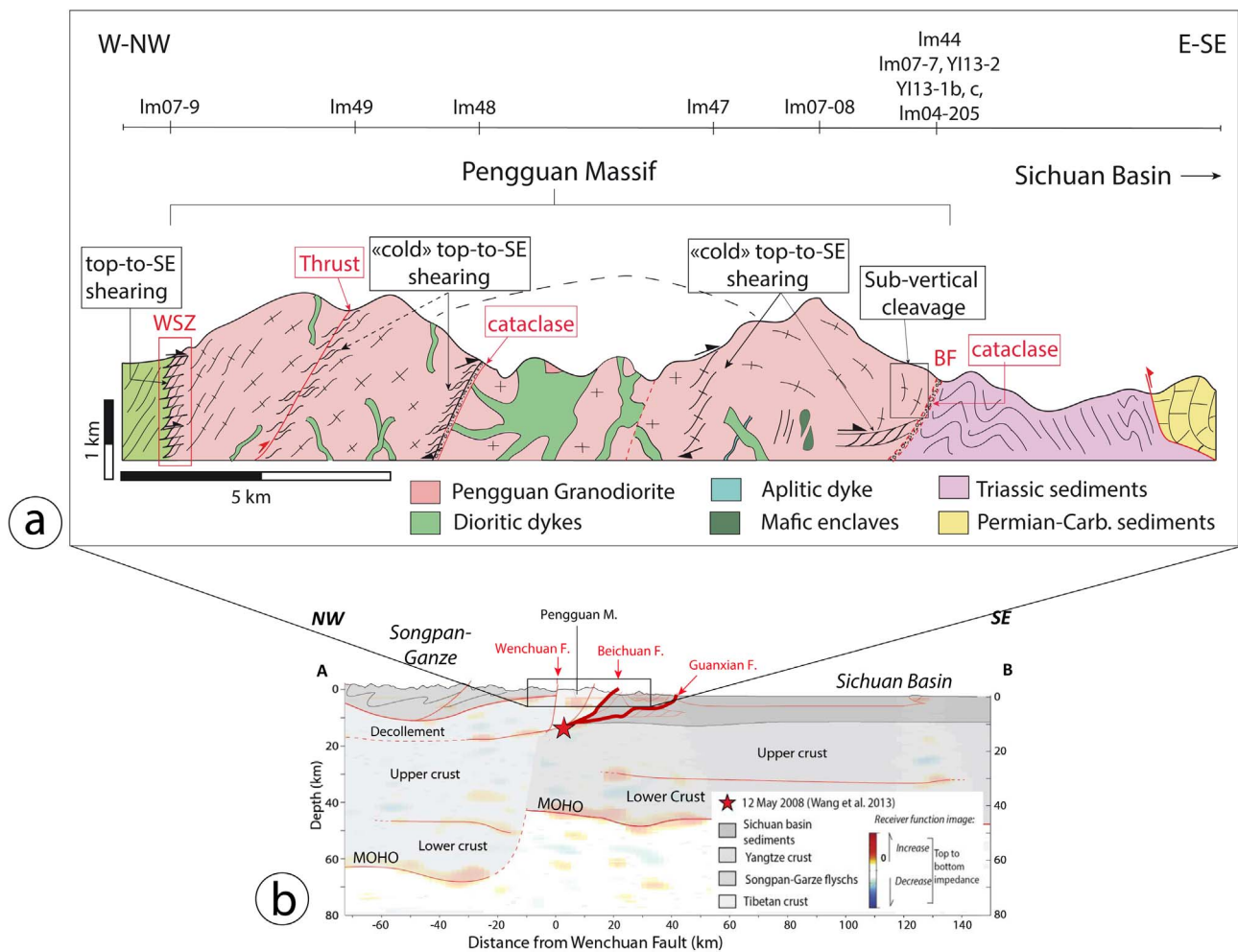


Fig. 2. (a) Schematic NW-SE cross section of the Pengguan massif showing the major structural and petrological features (see text for details). Location of studied samples and field localities projected on the cross section are also indicated (see Fig. 1). WSZ: Wenchuan Shear Zone, BF: Beichuan Fault. (b) Crustal section across the Eastern border of the Longmen Shan (see Fig. 1 for the location of the profile) imaged by receiver functions (modified from Robert et al., 2010b). The Wenchuan earthquake (red star) nucleated deeper than the junction between the Beichuan and Guanxian faults. Red lines indicate the fault segments that ruptured during the 2008 Wenchuan earthquake. (For interpretation of the references to colour in this figure legend, the reader is referred to the web version of this article.)

2.1. Studied area – the Pengguan massif

In the core of the LMS, bounded by the Wenchuan fault to the West and the Beichuan fault to the East, the South China basement crops out in the Pengguan massif (Figs. 1 and 2a). It consists of a combination of calc-alkaline granitoids (mostly granodiorites and diorites) yielding U-Pb ages of 827 ± 24 Ma (Billerot, 2011; Yan et al., 2008) emplaced in a context of Neoproterozoic active margin (de Sigoyer et al., 2014; Roger et al., 2008; Yan et al., 2008).

At large scale, both the basement and the cover of the Pengguan massif are folded into an anticline (Robert et al., 2010a, Figs. 1 and 2a). Deformation is observed in the massif close to the Beichuan fault, as well as in local shear zones, as reported in the schematic cross section of Fig. 2a. The majority of the shearing criteria observed in the field indicate a top-to-SE sense of shear.

Close to the WSZ, the Pengguan metagranitoid is mylonitized. C-S structures show a top-to-SE movement (Fig. 3f), with a cleavage (S) oriented at N40 NW60 (locality LM07-09 in Figs. 1 and 2a). Further North, close to the Wenchuan town (locality Im220 in Fig. 2a), in an equivalent structural position to locality LM07-09, the metagranitoid of the Pengguan massif is affected by a pervasive N25 W88 oriented cleavage in the proximity of the WSZ. The ductile deformation is underlined by a greenschist mineral assemblage of chlorite (chl) + epidote (ep). A doleritic dyke intrudes the metagranitoid and is

lately sheared along sub-vertical C' planes oriented N25 (locality Im221). In the mylonitic zone, abundant chlorite is aligned along the main cleavage. Chlorite is also observed in veins, associated to epidote, crosscutting the basic layers.

Moving southeastwards, at locality Im49 (Fig. 2a), the deformation affecting the Pengguan protolith is brittle and localized in a reverse fault oriented N50 NW60. Here the metagranite is cross cut by an epidote-rich metadoleritic dyke. Eastwards (locality Im48 in Fig. 2a), another zone of localized deformation is observed. At this location, the deformation is ductile and characterized by C' -S structures. C' planes are oriented N65 NW75 and the associated sigmoid structures shows a top-to-SE sense of shear. Further North, in an equivalent structural position, metagranite is mylonitized and cross cut by late N02 E76-oriented dextral strike slip faults (locality Im219, see Fig. 1 for its location).

Approaching the BF, (locality Im47 in Fig. 2a) the deformation becomes more pervasive. Chlorite and epidotes are aligned along C' planes oriented N53 W75 (Fig. 4m, n and o). Sigmoid structures reveal a top-to-SE sense of shear. Deformation is particularly localized at the lithological boundaries between metagranites and metabasites, both extensively cross cut by epidote-rich veins. The Beichuan fault zone becomes tighter close to Yingxiu village (localities Im44, Y113-2, Y113-1b and c, Im07-8 and 7 in Fig. 2a) where the fault trace is underlined by a topographic step due to lithological differences between the crystal-

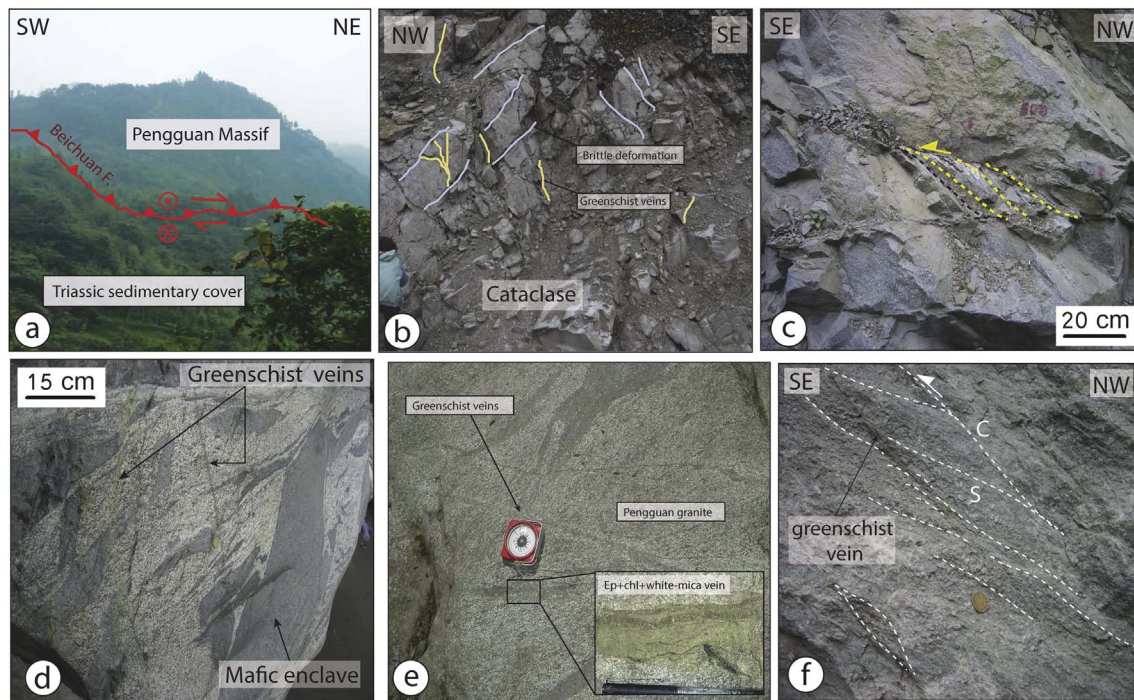


Fig. 3. Photographs of the field structures observed in the Pengguan massif. (a) Close to Yingxiu village, the Beichuan fault separates the metamorphic crystalline rocks of the Pengguan massif (basement) in the hanging wall of the fault to the North-West from the non-metamorphic Triassic sedimentary cover in the footwall to the South-East. (b) Close to Yingxiu village the Pengguan massif appears strongly cataclased and crosscut by green schist metamorphic veins. (c) Metagranite close to the Beichuan fault showing a combination of ductile top-to-SE structures and brittle fractures. (d) Mafic enclaves stretched during granite emplacement and cross cut by green schist metamorphic veins. (e) Green schist-facies metamorphic veins crosscutting the Pengguan crystalline rocks in the Lanjiaping area. Inset shows the epidote + chlorite + white mica + quartz-bearing green schist-facies equilibrium assemblage observed in the veins. (f) top-to-SE C-S structures and chlorite + epidote + white mica green schist-facies veins in the metagranite of the Pengguan massif close to the WSZ.

line basement of the Pengguan massif to the NW and the Triassic sedimentary cover to the SE (Fig. 3a). In the hanging wall of the fault, the Pengguan massif is strongly cataclased according to two perpendicular planes (sub-vertical planes oriented N83 S75 and sub-horizontal planes) (Fig. 3b). Locally ductile C/S structures are underlined by a steeply NW dipping cleavage and the development of cm-scale green schist facies shear zones ('cold shearing' in Figs. 2a and 3c). At locality lm07-8, the metagranodiorite and the metabasic dykes are sheared with a top-to-SE movement. Green schist metamorphic veins of chl + ep + white mica + quartz (qtz) oriented at N75 SE55 cross-cut the granite.

Within the Beichuan fault zone, there are few NE-SW trending lineations parallel to the fault strike, reflecting the strike slip component of the Beichuan fault. Structures similar to the ones described just above are identified along the northern prolongation of the BF, in the proximity of the Lanjiaping village (Fig. 1). In this zone the Pengguan massif is affected by brittle-ductile deformation associated with the development of NW dipping cleavage (S1 in Fig. 1). Brittle cracks are oriented N92 N30 and filled with epidotes, chlorite and muscovite. Their orientation is compatible with the tension cracks associated with the strike slip component of the Beichuan fault. Mafic enclaves are stretched during the emplacement of the magmatic complex, as shown by their blurred contacts with the surrounding metagranitoids. They are sheared along planes oriented at N38 NW50 and overprinted by metamorphic veins containing chl + ep + wm + qtz (Fig. 3d). Green schist-facies veins of chl + ep + white mica + qtz of 5 to 20 cm in width cross cut the metagranitoid (Fig. 3e).

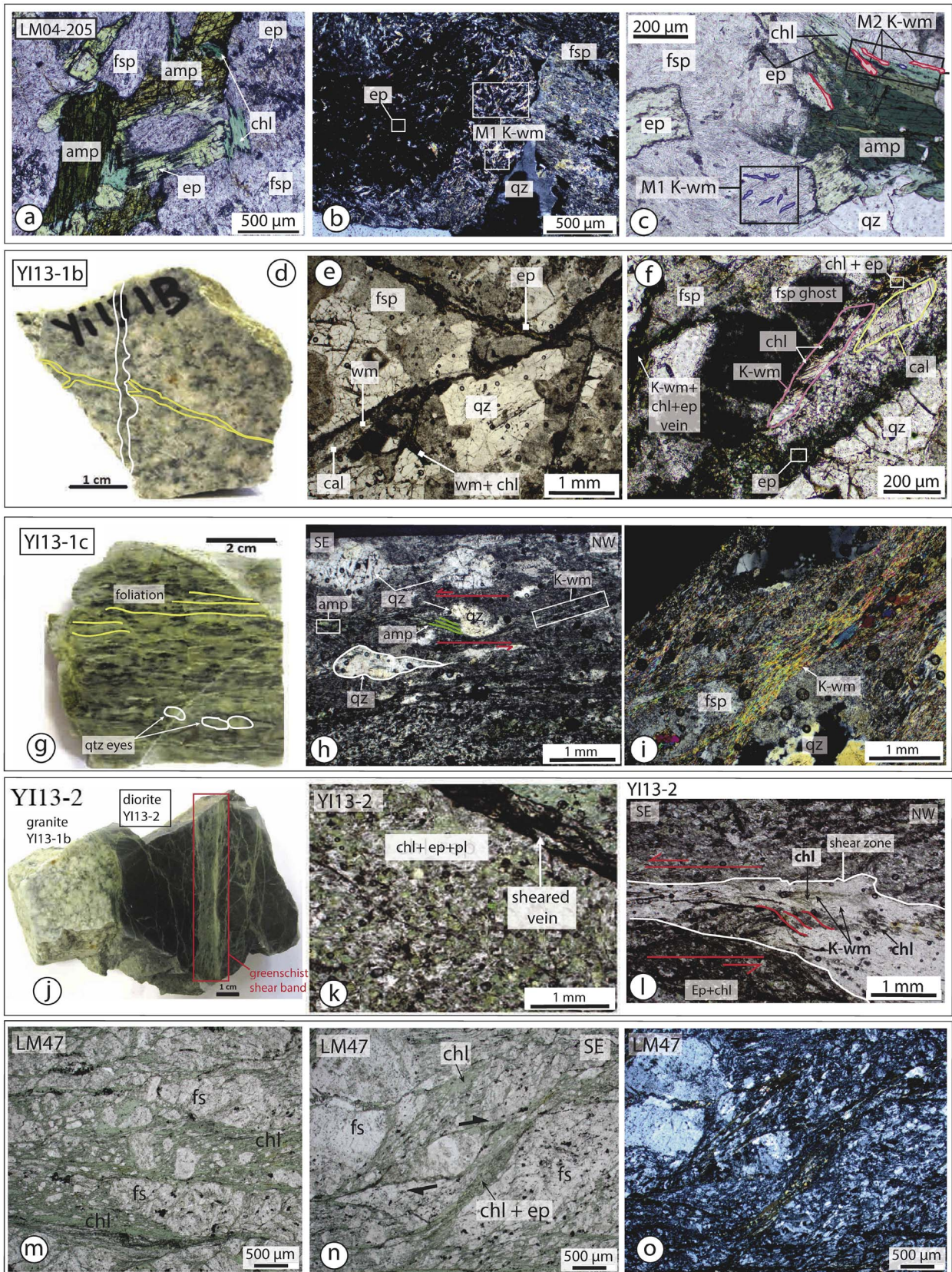
While our petrological observations attest for the thrusting component on the Beichuan fault through time, the few NE-SW oriented lineations and E-W oriented cracks observed close to the fault reflect its strike slip component. Both components were recorded during the last earthquakes on the Beichuan fault (Wu et al., 2014; Fielding et al., 2013; de Michele et al., 2010a,b; Liu-Zeng et al., 2009) and are therefore characteristic of the fault.

The sampling areas of this study are located near the villages of Yingxiu and Lanjiaping, 15 km NW and 70 km NE of the town of Dujiangyan respectively (white dots in Fig. 1).

3. Sampling

Samples were collected in the hanging wall of the Beichuan fault where the Pengguan massif crops out. Samples of three different lithologies (meta-granite, meta-granodiorite, meta-diorite) qualitatively showing different intensities of deformation were collected in order to track the possible influence of the chemistry of the protolith and of the intensity of deformation on metamorphic assemblages. All studied samples showed a magmatic paragenesis (protolith) overprinted by a green schist facies metamorphic assemblage. The green schist index minerals are generally aligned along the main cleavage (i.e. Fig. 4m, n and o), in fractures (i. e. Fig. 4e and f) or at the lithological boundaries. Within this framework a subset of five samples were selected which contained enough K-white micas and chlorite of an adequate size ($\geq 15\text{--}20\ \mu\text{m}$) to perform systematic chemical analyses, thermobarometric estimates and $^{40}\text{Ar}/^{39}\text{Ar}$ dating at a spatial resolution of $\sim 80\ \mu\text{m}$. The exact location of samples is given in Fig. 1 and Table 1.

Samples LM04-205 and LM04-206 are weakly-deformed meta-granodiorites collected in the Lanjiaping sector, a few kilometers from the Beichuan fault (Fig. 1). The original magmatic assemblage is composed of subehedral crystals of K-feldspar, plagioclase, quartz and amphibole of $> 500\ \mu\text{m}$ in length (Fig. 4a and c). Amphibole is green-brownish and strongly pleochroic. At the grain boundary between amphibole and plagioclase, chlorite and yellow-greenish epidote flakes of $200\ \mu\text{m}$ in size crystallized (Fig. 4a and c). Plagioclase has broken down into albite + epidote microcrystals to form dark bush-like shapes. Under cross-polarized light K-feldspar is hardly recognizable since it is extensively replaced by randomly oriented K-white mica $15\text{--}30\ \mu\text{m}$ in size (M1-K-white micas in Fig. 4b and c). At the grain boundary between albite and chlorite, K-white micas of $200\ \mu\text{m}$ develop (M2-K-



(caption on next page)

Fig. 4. Macroscopic and microscopic views of samples selected for this study under cross polarized (b, i, o) and uncrossed polarized light (c, e, f, h, i, k, l, m, n). Abbreviations from Whitney and Evans (2010). K-wm: K-white mica. (a) Optical image of the meta-granodiorite LM04-205. At the grain boundary between amphibole and feldspar (albite), a greenschist-facies assemblage of epidote + chlorite crystallized. (b) Zoom of the top-left side of the microphotograph in -a. Albite is overprinted by epidote and M1K-white mica (see the text for details). (c) Epidote and chlorite crystallizing at magmatic amphibole rims in sample LM04-205. Blue: M1K-white mica (K-wm). Red: M2K-wm (see the text for details). (d) Mesoscale view of the meta-granite Y113-1b showing two perpendicular greenschist veins. (e) Two types of greenschist veins in thin section of sample Y113-1b. (f) Zoom of the bottom-left side of the picture -e, showing a vein filled with large crystals of K-white mica, epidote and calcite. (g) Deformed meta-granodiorite Y113-1c presenting a strong horizontal foliation underlined by greenschist metamorphic minerals and feldspar eye-shaped porphyroblasts. (h) Sample Y113-1c at thin section scale. K-wm develop in quartz pressure shadows and in the main foliation. (i) Crossed polar image of the K-white micas oriented along the main foliation in sample Y113-1c. (j) Shear zone at the sample-scale in meta-dioritic dyke (sample Y113-2) intruding the Pengguan meta-granite Y113-1b. (k) Sample Y113-2 at thin section scale. (l) K-white mica and chlorite-bearing shear bands in sample Y113-2. (m) Cataclased feldspar embedded in the chlorite-rich matrix in sample lm47. (n) Sample lm47: chl + ep cleavage domains alternate with fractured feldspar grains. (o) Cross polarized image of Fig. 4n. (For interpretation of the references to colour in this figure legend, the reader is referred to the web version of this article.)

white mica in Fig. 4c). They present irregular borders with albite and sharp borders with chlorite. No magmatic K-white mica was observed in the protolith, and in particular the only M2-K-white mica group was observed in association with chlorite. This suggests that M2-K-white micas are the result of the metamorphic overprint. M2-K-white mica, chlorite and epidote are then considered as index minerals of the greenschist facies metamorphism in the Pengguan samples.

Sample Y113-1b is a more deformed metagranite from the Yingxiu sector (Fig. 4d). The magmatic assemblage is made of subeuhedral grains of quartz, albite and small relics of biotite 50–100 µm in size (Fig. 4e). Within albite grains dark patches of micrometric epidote develop (Fig. 4e). Yellow-greenish epidote and chlorite grew at biotite grain boundaries. Two perpendicular generations of greenschist veins crosscut the magmatic texture (Fig. 4d and e). One is filled with aggregates of yellow epidotes (15 µm in size); the other contains greenish epidote, 200 µm K-white mica grains, chlorite and large crystals (200 µm) of calcite (Fig. 4f).

Sample Y113-1c is a strongly foliated meta-granodiorite from the Yingxiu sector (Fig. 4g). The foliation underlined by oriented grains of K-white mica (Fig. 4i), light green amphibole (actinolite) and small quartz grains (Fig. 4h). Larger grains of quartz are stretched, showing tails formed by pressure dissolution-recrystallization or are broken in smaller grains to form sigma-shaped eye porphyroblasts showing a top-to-SE sense of movement (Fig. 4h). Actinolite and K-white mica developed in pressure shadows around the quartz porphyroblasts. Albitic feldspar is sericitized, creating a dusty aspect (Fig. 4h). When partially preserved, it is broken in small grains. The brittle deformation of feldspar and the brittle-viscous deformation of quartz suggest temperature < 450 °C (Sibson, 2001) and close to 280 ± 30 °C (Stöckhert et al., 1999).

Sample Y113-2 is an intensely deformed meta-dioritic dyke intruding the granite Y113-1b (Fig. 4j). At the sample scale a greenschist shear band of 1 cm width cross-cuts the metadiorite (Fig. 4j). The metadiorite is composed of epidote, chlorite and plagioclase (Fig. 4k). In the shear band chlorite crystallized in association with K-white mica grains of 100–200 µm (Fig. 4l). Mica and chlorite preferred orientation suggests a top-to-the-SE sense of shear.

In our samples K-rich white micas were observed in two different structural positions: (i) as 15 µm grains within feldspar (M1-K-white mica, Fig. 4b and c) and (ii) as 100–200 µm grains at the biotite/chlorite feldspar grain boundary, filling the greenschist veins, within the main foliation or in greenschist shear bands (M2-K-white micas, Fig. 4c, f, i, l). A high-resolution petrological approach was adopted to resolve the possible chemical differences between the two families of K-white micas. This approach ran through two successive stages: (i)

chemical maps of metamorphic minerals were realized with an Electron Probe Microanalyser (EPMA) in order to study the relationships between their chemical heterogeneities and rock microstructures; (ii) thermodynamic computations were performed to estimate P-T conditions of crystallization of analyzed metamorphic minerals. Metamorphic white mica were then dated to constrain the timing of their growth.

4. Analytical methods

4.1. EPMA analyses

Quantitative compositional X-ray maps were acquired on selected chlorite and K-white mica-rich areas on the JEOL JXA-8230 at the Institut des Sciences de la Terre (ISTerre Grenoble). The mapping conditions were 15 keV accelerating voltage and 100 nA specimen current. High quality point analyses were also acquired at conditions of 15 KeV and 12 nA. The raw compositional maps were transformed into quantitative maps of oxide wt% using XMapTool software (Lanari et al., 2014a) based on point analyses of all phases identified in the mapped area. XMapTools software, was also partly used to calculate mica and chlorite structural formulae for each pixel of the mica and chlorite quantitative maps. Compositional maps (in p.f.u. and end-member fraction) were then extracted for a single mineral phase in order to track small chemical heterogeneities and their relationships with the microstructural position.

4.2. Chlorite and K-white mica thermobarometry

For each chlorite analysis performed at EPMA temperature was estimated using the chlorite-quartz-water multi-equilibrium thermobarometric method (Vidal et al., 2006; Lanari et al., 2012). The temperature of chlorite crystallization depends on the activity of solid solution components of the chlorite phase in equilibrium with quartz and water (Vidal et al., 2005, 2006). A convergence of the equilibria among all these components was reached for a minimal X_{Fe}^{3+} of chlorite, at given initial pressures of 5–6 kbar, in agreement with the white mica multi-equilibrium results. Convergence was considered to be achieved when the temperature difference between all equilibria was less than 30 °C. Since carbonates were observed in the granites from Yingxiu sector, calculations were performed for a variable water activity ranging from 0.5 to 1. No relevant shift in temperature was observed with variations in water activity.

Pressure was calculated using a method that models mica compositional variation as a function of P and T (Parra et al., 2002; Dubacq

Table 1
Location and lithological characteristics of samples collected for thermobarometry.

Sample	Lithology	Latitude	Longitude	Elevation	Magmatic assemblage	Metamorphic assemblage
LM04-205	Metagranodiorite	N31.36225	E104.02632	849 m	fs + plg + Qtz + amph + sph	ep + chl + K-wm
LM04-206	Metagranodiorite	N31.35285	E104.03128	855 m	fs + plg + Qtz + amph + sph	ep + chl + K-wm
Y113-1b	Metagranite	N31.03585	E103.28477	916 m	fs + plg + Qtz + bt	ep + chl + K-wm + calcite
Y113-1c	Metagranodiorite	N31.03584	E103.28480	920 m	plg + Qtz + amph	K-wm + amph (actinote)
Y113-2	Metadiorite	N31.03586	E103.28476	937 m	plg + amph	ep + chl + K-wm

et al., 2010). For each white-mica analysis a P-T line representing the conditions of equilibrium among quartz + water + K-white mica was drawn. Along this line the interlayer water content of the mica varied. Pressure was then estimated at given temperature (e.g. the temperature obtained from chlorite-quartz-water thermometry) assuming thermodynamic equilibrium between chlorite, white mica and quartz (Lanari et al., 2012). Finally equilibria between couples of chlorite and M2-K-white mica were tested simultaneously with the combined approach of Vidal et al. (2006) and Dubacq et al. (2010) as an independent check for the estimated P-T equilibrium conditions. Only the solutions with a maximum residual lower than 100 kJ were accepted.

4.3. $^{40}\text{Ar}/^{39}\text{Ar}$ dating

Metamorphic K-white micas were dated by laser ablation $^{40}\text{Ar}/^{39}\text{Ar}$. *In-situ* laser ablation allowed the ages to be linked to chemical heterogeneities within micas in different microstructural positions (see Section 4.1).

Thick sections of 1 mm thick and 1 cm × 1 cm size were made from the mirror-image chips of those used to make the analyzed thin sections. Samples were irradiated at the TRIGA reactor in Pavia (Italy). The analyses were performed in the $^{40}\text{Ar}/^{39}\text{Ar}$ laboratory of Montpellier University (France) using a UV Nd-YAG (Spectrum Laser System) laser operating at a wavelength of 266 nm and beam diameter of 80 μm. Spot analyses and 120–500 μm long profiles were performed in order to obtain ^{40}Ar signals at least 5 times greater than blank values. Following clean up the gas was collected in Thermo-Scientific Argus VI mass spectrometer for isotopic analysis. System blanks were run every two sample analyses and were then subtracted from the sample signals. $^{40}\text{Ar}/^{39}\text{Ar}$ ages were calculated with the age equation of Min et al. (2000), considering a J value of 0.0041072 and an atmospheric ratio $^{40}\text{Ar}/^{36}\text{Ar}$ of 295.50 ± 1.03 (Steiger and Jäger, 1977). $^{38}\text{Ar}/^{39}\text{Ar}$ and $^{37}\text{Ar}/^{39}\text{Ar}$ were also estimated in order to exclude contamination by calcic or chlorine-bearing minerals phase(s).

5. Results

5.1. Chemical results

5.1.1. Chlorite

In all studied samples chlorite is associated with the M2-K-white mica group (see Section 3 and 6.1) and shows a preferred orientation in the shear zones of the strongly deformed diorite YI13-2. Chemical analyses for chlorite of samples from both studied sites are reported in Table 3. The X_{Mg} content of chlorite in more deformed samples (YI13-1b and in the YI13-2) ranges between 0.62 and 0.65 for a Si (p.f.u.) content of 2.61–2.8 (Fig. 5). Chlorite in the less-deformed granitoids (LM04-205 and LM04-206) contains higher X_{Mg} , ranging from 0.66 to 0.74 for a Si (p.f.u.) content of 2.79–2.90 (Fig. 5). The different

chemical composition of chlorite may be partly due to the different bulk rock compositions (Lanari et al., 2014b). However only one homogenous chemical generation of chlorite is clearly identified within each sample, suggesting a continuous evolution of the chlorite chemical composition during its crystallization. No chlorite was observed in sample YI13-1c.

5.1.2. Two generations of K-white mica

Two groups of white micas were observed in the samples from the Pengguan massif, in different microstructural positions (see Section 3). They can be distinguished from their chemical composition revealed by the X-ray chemical maps (Fig. 6b, c, e, f). Significant chemical variations involve the celadonite and muscovite contents of the mica solid solution. Representative mica compositions are reported in Table 2.

In less-deformed meta-granodiorites LM04-205 and LM04-206 X-ray maps show M1-K-white micas of micrometric size located within K-feldspar grains (M1 in Fig. 6a–c). This generation is characterized by a low celadonite content ranging between 0.08 and 0.19 (fraction) for a muscovite content of 0.58–0.83 (Fig. 6a–c). At M1 mica rims the celadonite content increase at 0.27–0.35 suggesting a second phase of crystallization at higher pressure (for a given temperature) than M1 (Fig. 6b and c). A second (M2) K-white mica group is recognized in flakes of ca. 100 μm observed in equilibrium with chlorite. The M2 generation contains a higher celadonite content ranging from 0.21 to 0.45 for a lower muscovite content comprised between 0.45 and 0.65 (Fig. 6a and b).

In deformed samples YI13-1b, YI13-1c and YI13-2 only one chemical group of K-white mica was observed in agreement with microstructural observations at thin section scale. This group is characterized by a celadonite content of 0.25–0.40 for a muscovite content of 0.35–0.60 (Fig. 6d–f). The chemical composition of K-white micas of the more deformed samples is very close to the M2 generation in less-deformed ones. In deformed samples, the M2 mica largely prevails (in association with chlorite) suggesting that the M2 generation is associated with the greenschist-facies metamorphic event.

5.2. P-T estimates

The chlorite-quartz-water multi-equilibrium method of Vidal et al. (2005, 2006) was applied to each pixel of chlorite selected on the X-ray compositional maps (see Section 4.2). For low deformed granitoids (LM04-205 and LM04-206), the calculated temperature ranges between 260° and 320 °C, while for more deformed samples (YI13-1b and YI13-2) the temperature ranges between 260 °C and 300 °C (Fig. 7a). No chlorite was observed in the meta-granodiorite YI13-1c. We therefore suggest that the chlorite crystallized in this sample in the same range of temperature than in the surrounding meta-granite (YI13-1b) and meta-diorite (YI13-2).

Similarly to chlorite, the phengite-quartz-water method of Dubacq et al. (2010) was applied to each pixel of M1 and M2 mica groups selected on the X-ray map (see Section 4.2). The results are plotted in Fig. 7b for all studied samples. Pixels selected from the cores of M1 group show temperature of 360°–430 °C ($P = 5\text{kbar}$). In contrast pixels selected from the rims of M1 group and from the M2 group show temperatures lower than 310 °C at the same fixed pressure (Fig. 7b).

Following the technique described in Lanari et al. (2012) P-T equilibrium conditions of the greenschist overprint were then estimated from the intersection of the mica-quartz-H₂O and chl-quartz-H₂O equilibria obtained for M2K-white mica group and chlorite since they are considered to have crystallized at the thermodynamic equilibrium. Estimated P-T conditions yield at 290 ± 20 °C, 6.5 ± 1 kbar for samples LM04-205 and LM04-206 and at 280 ± 20 °C, 7 ± 1 kbar for samples YI13-1b, YI13-1c and YI13-2 (Fig. 7b).

Results of equilibrium calculations between couples of chlorite and K-white mica analyses are summarized in Fig. 7c (for the tested sample

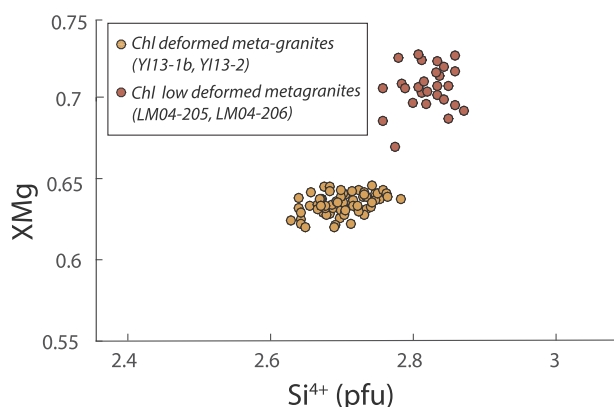


Fig. 5. Chlorite chemical analyses represented in a Si^{4+} (p.f.u.) vs X_{Mg} diagram.

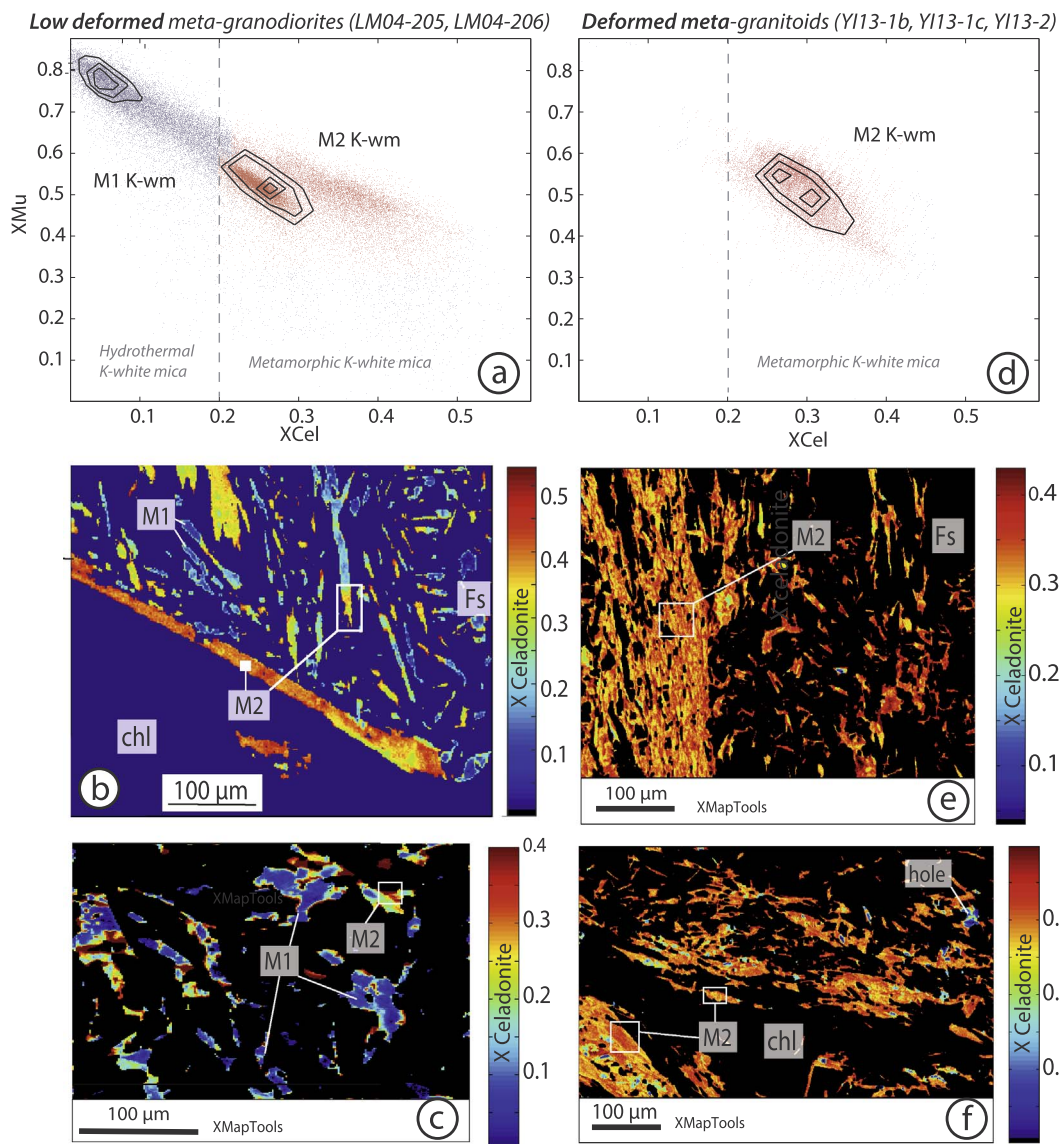


Fig. 6. Xceladonite (XCel) vs Xmuscovite (XMu) diagram of K-white micas (K-wm) for all studied samples and corresponding X-ray maps of celadonite content. Solid lines in panel a and d indicate density contours for K-white mica analyses. (a) XMu vs XCel diagram of K-wm analyses for samples LM04-205 and LM04-206. Two chemical groups of K-wm are identified. (b) X-ray map of the celadonite content in K-wm of sample LM04-205. M1: M1-K-wm, M2: M2-K-wm. (c) Zoomed X-ray map of M1-K-wm grains developing within K-feldspar grains. (d) XMu vs XCel diagram of K-wm in deformed meta-granitoids YI13-1b, YI13-1c and in meta-diorite YI13-2. One family of K-wm (M2) is observed. (e) X-ray map of the celadonite content in K-wm stretched in the main foliation of sample YI13-1c. (f) X-ray map of the celadonite content of K-wm developed in association with chlorite in the shear band of meta-diorite YI13-2.

YI13-1b). No equilibria between chlorite and M1K-white micas were reached. On the contrary, equilibria were reached between chlorite and M2-K-white micas at 7 ± 1 kbar, 280 ± 30 °C, in good agreement with P-T conditions estimated separately for chlorite and micas.

5.3. $^{40}\text{Ar}/^{39}\text{Ar}$ dating on white micas

In situ $^{40}\text{Ar}/^{39}\text{Ar}$ dating was performed on deformed samples of the Pengguan massif where only the M2 mica group was well expressed, in order to avoid mixing ages due to inherited Ar residing in the relics of the older M1K-white mica generation. Among the selected samples only one, the meta-granodiorite YI13-1c, presented K-white mica bands large enough ($> 80 \mu\text{m}$ wide) to be dated in situ by $^{40}\text{Ar}/^{39}\text{Ar}$ laser ablation. All the analyses performed on sample YI13-1c are listed in Table 4. An example of ablated surface is provided in Fig. 8. Ages cluster around an average age of 137 ± 3 Ma (lower Cretaceous). No contamination by calcite or chlorine-bearing mineral phases were noted by the calculated the $^{38}\text{Ar}/^{39}\text{Ar}$ and $^{37}\text{Ar}/^{39}\text{Ar}$ ratios.

6. Discussion

6.1. Syn-greenschist metamorphism genesis of the M2 white mica

Two generations of K-white mica were observed in the metagranite and metagranodiorite of the Pengguan crystalline massif sampled in the hanging wall of the Beichuan fault. The first one (M1-K-white mica group) is related to the alteration of feldspar, since it is never associated to deformation or to other index metamorphic minerals. Moreover, hydrothermal allanites (REE-rich epidotes) are observed in samples YI13-1b and YI13-1c. An attempt of dating these allanites with the in situ U-Pb/Th laser ablation technique was carried out (unpublished results). Despite of the scatter, preliminary results, show that ages cluster around 650–750 Ma (Figs. 1 and 2 in Supplementary material). This suggests that the Pengguan massif was exposed to a post-magmatic hydrothermal alteration, which may mark the timing of crystallization of M1K-white mica at the expense of K-feldspar.

The M2-K-white mica group is always associated with other

Table 2
Representative chemical analyses for K-white mica for all studied samples. K-wm: K-white mica. X_{cel} = celadonite fraction, X_{mus} = muscovite fraction, X_{pyr} = pyrophyllite fraction, X_{par} = paragonite fraction.

Sample	LM04-205		LM04-206		YI13-1b	YI13-1c	YI13-2
	K-wm ₁	K-wm ₂	K-wm ₁	K-wm ₂	K-wm ₂	K-wm ₂	K-wm ₂
SiO ₂	45.56	47.65	44.44	47.09	53.61	50.09	52.16
TiO ₂	0.04	0.03	0.03	0.09	0.02	0.1	0.03
Al ₂ O ₃	34.69	28.72	34.67	27.63	27.19	27.29	29.58
FeO	2.59	5.80	2.37	4.94	2.47	2.8	4.31
Fe ₂ O ₃	0.00	0.00	0.00	0.00	0.00	0.00	0.00
MnO	0.05	0.05	0.05	0.06	0.04	0.02	0.09
MgO	0.82	2.16	0.67	2.09	3.78	3.61	2.91
CaO	0.06	0.06	0.07	0.07	0.01	0.03	0.05
Na ₂ O	0.15	0.13	0.14	0.12	0.04	0.1	0.01
K ₂ O	8.91	9.57	8.95	9.19	8.31	9.4	8.21
Total	92.87	94.17	91.39	91.27	95.47	93.44	97.36
Cations							
Si	3.07	3.20	3.04	3.25	3.51	3.39	3.34
Ti	0.00	0.18	0.00	0.18	0.00	0.01	0.00
Al	2.75	2.27	2.80	2.25	2.10	2.18	2.23
Fe ⁺²	0.13	0.30	0.12	0.26	0.12	0.14	0.21
Mn	0.00	0.00	0.00	0.00	0.00	0.00	0.01
Mg	0.08	0.22	0.07	0.22	0.37	0.36	0.28
Ca	0.00	0.00	0.01	0.01	0.00	0.00	0.00
Na	0.02	0.02	0.02	0.02	0.01	0.01	0.00
K	0.76	0.82	0.78	0.81	0.69	0.81	0.67
Total	6.87	6.89	6.87	6.86	6.75	6.87	6.76
End-members							
X_{mus}	0.68	0.52	0.71	0.51	0.41	0.49	0.47
X_{cel}	0.14	0.35	0.12	0.35	0.33	0.35	0.30
X_{pyr}	0.16	0.11	0.15	0.12	0.25	0.15	0.23
X_{par}	0.01	0.01	0.01	0.01	0.00	0.01	0.00

Table 3
Representative analyses of chlorite for all studied samples.

Sample	LM04-205	LM04-206	YI13-1b	YI13-2
SiO ₂	27.82	27.85	27.77	27.62
TiO ₂	0.03	0.05	0.01	0.01
Al ₂ O ₃	18.36	18.63	20.33	21.55
FeO	16.39	17.28	20.95	20.90
Fe ₂ O ₃	0.00	0.00	0.00	0.00
MnO	0.44	0.50	0.41	0.55
MgO	21.10	22.27	18.49	18.53
CaO	0.05	0.07	0.02	0.02
Na ₂ O	0.03	0.03	0.01	0.01
K ₂ O	0.02	0.02	0.01	0.01
Total	84.24	86.70	88.00	89.20
Cations				
Si	2.81	2.75	2.72	2.68
Ti	0.18	0.18	0.18	0.18
Al	2.19	2.17	2.34	2.46
Fe ⁺²	0.87	0.90	1.08	1.06
Fe ⁺³	0.37	0.38	0.46	0.45
Mn	0.04	0.04	0.03	0.05
Mg	3.18	3.27	2.70	2.66
Ca	0.01	0.01	0.00	0.00
Na	0.01	0.01	0.00	0.00
K	0.00	0.00	0.00	0.00
Total	9.47	9.53	9.34	9.35
XMg	0.72	0.72	0.64	0.64

greenschist-facies metamorphic minerals (chlorite, epidote, albite) and is related to the main deformation, as shown in by the M2 grains elongated in the main cleavage in Fig. 4g, h, i, j, l, m, n and o. The M2 mica group is more developed in strongly deformed samples.

These observations suggest that the M2 white micas are related to a greenschist facies metamorphic event and not to a second hydrothermal alteration event. This interpretation is supported by the fact that similar

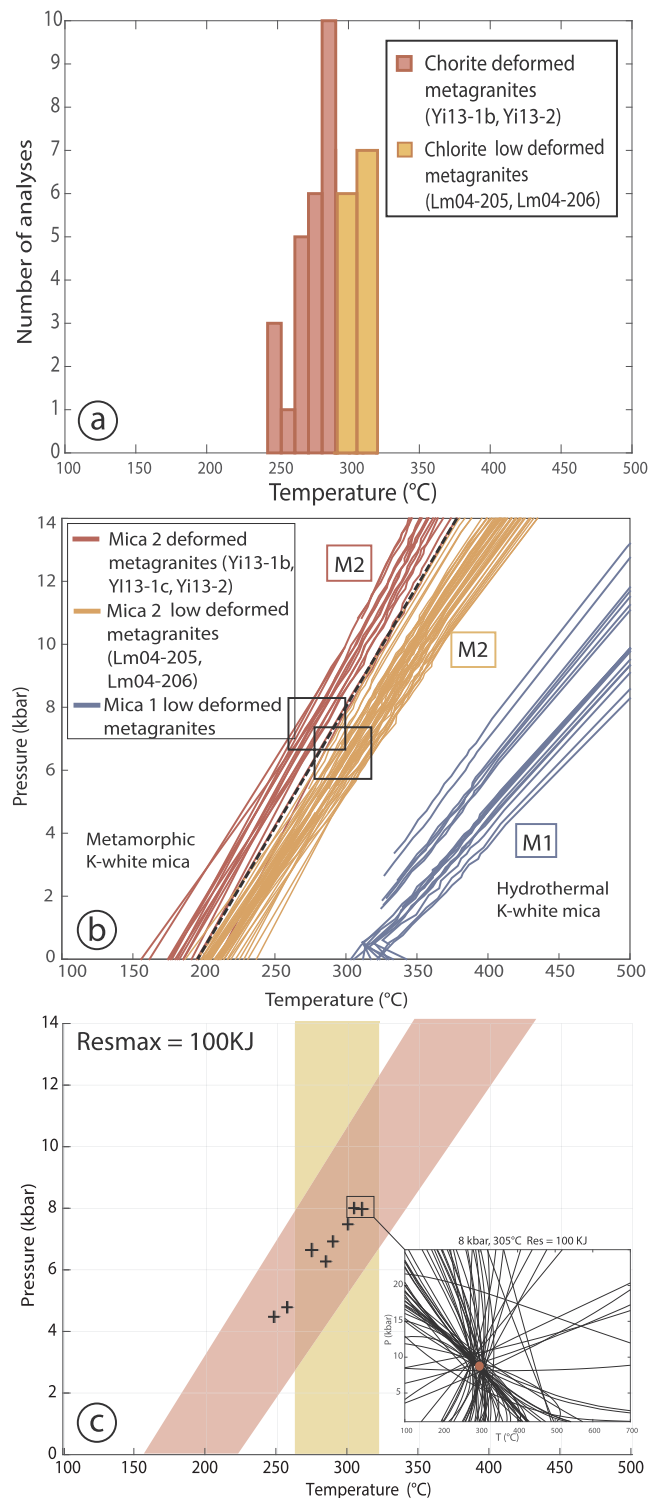


Fig. 7. Thermobarometric estimates. (a) Temperature estimated from chl-qtz-H₂O multi-equilibrium method (Vidal et al., 2006) for low-deformed meta-granodiorites (orange) and more deformed samples (red). (b) K-white mica equilibrium lines obtained with the mica-qtz-H₂O multi-equilibrium method (Dubacq et al., 2010). M2-K-wm P-T lines are marked in red and orange. M1-K-wm P-T lines are marked in blue. Boxes indicate the interval for estimated P-T conditions. (c) P-T estimates obtained by chlorite-M2K-wm multi-equilibrium modelling (sample YI13-1b). The insert shows an example of equilibrium conditions constrained by the intersection of the chl-K-wm-qtz-H₂O reaction lines at a unique point (P-T conditions), for a maximum residual of 100 kJ. (For interpretation of the references to colour in this figure legend, the reader is referred to the web version of this article.)

Table 4
Ages obtained by in situ $^{40}\text{Ar}/^{39}\text{Ar}$ technique and their uncertainties, for the deformed meta-granodiorite Y113-1c.

Sample	^{36}Ar [V]	%1 σ	^{37}Ar [V]	%1 σ	^{38}Ar [V]	%1 σ	^{39}Ar [V]	%1 σ	^{40}Ar [V]	%1 σ	$^{40}\text{Ar}/^{39}\text{Ar}$ (k)	$\pm 2\sigma$	Age (Ma)	$\pm 2\sigma$	$^{40}\text{Ar}(\%)$	$^{39}\text{Ar}(\%)$
Y113-1c-1	0.0034859	81.972	0.1163530	102.412	0.0282156	68.447	0.983524	2.552	21.26014	2.570	20.57149	± 2.29935	146.67	± 15.75	95.16	5.76
Y113-1c-2	0.0058108	49.462	0.2474693	36.865	0.0105392	229.731	0.962566	1.725	18.76168	2.910	17.72294	± 2.18555	127.06	± 15.13	90.91	5.63
Y113-1c-3	0.0026523	109.127	0.2718683	39.281	0.0400728	60.316	1.773981	1.163	35.91837	1.520	19.81132	± 1.23360	141.46	± 8.47	97.84	10.39
Y113-1c-4	0.0031845	54.647	0.0074125	906.052	0.0680420	88.997	2.418757	0.977	47.22835	0.261	19.12784	± 0.57532	136.76	± 3.96	97.96	14.16
Y113-1c-5	0.0043521	40.551	0.0856113	94.010	0.0451038	129.189	2.142984	0.977	42.96563	0.288	19.43587	± 0.62816	138.88	± 4.32	96.94	12.55
Y113-1c-6	0.0040720	43.132	0.7733966	11.200	0.0169980	364.992	1.896127	1.229	39.32652	0.313	20.13683	± 0.74964	143.70	± 5.14	97.06	11.10
Y113-1c-7	0.0007348	374.332	0.2085370	132.636	0.0526962	46.973	2.544005	2.630	47.07291	1.730	18.58743	± 1.33227	133.04	± 9.19	100.45	14.89
Y113-1c-8	0.0027434	100.718	0.1677339	163.882	0.0339074	70.272	1.997579	3.362	36.52390	2.230	17.87690	± 1.66709	128.13	± 11.53	97.77	11.70
Y113-1c-9	0.0023845	115.402	0.3498243	79.225	0.0559389	47.381	2.361166	2.864	43.30495	1.881	18.04721	± 1.42109	129.30	± 9.83	98.39	13.82

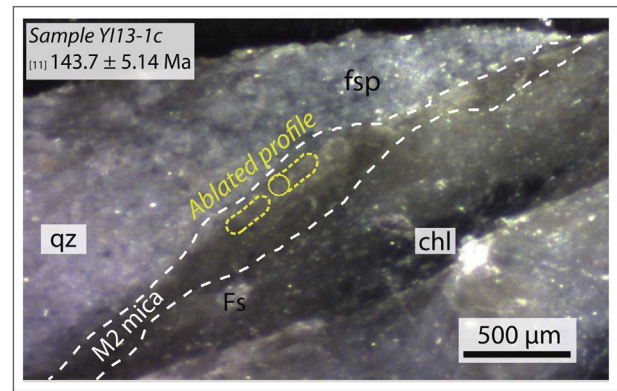


Fig. 8. Reflected light image of M2K-white mica bands in sample Y113-1c, oriented along the main cleavage (dashed white contour). An example of the profile ablated by the UV-laser (for $^{40}\text{Ar}/^{39}\text{Ar}$) is shown in yellow.

P-T conditions are retrieved for the M2 mica-chlorite assemblage for localities over 70 km away (Yingxiu and Lanjiaping areas, Fig. 1). Hence, P-T conditions are more likely to reflect a regional metamorphic overprint than local hydrothermal fluid circulation. Furthermore, $^{40}\text{Ar}/^{39}\text{Ar}$ ages suggest that white mica formed at ~ 137 Ma. It is difficult to explain an intensive large-scale circulation of hydrothermal fluids accompanied by deformation occurring at ca. 137 Ma, more than 600 Ma after the granite emplacement (ca. 800 Ma), without evoking a regional-scale metamorphic event.

6.2. Reliability of petrological and thermobarometric results

Thermobarometric estimates were performed with an inverse modelling approach, which calculates fractions among K-white mica and chlorite solid solution end-members allowing to be exempted from the chemical effect of the different lithologies. Therefore, in the same sample, chlorite from different chemical domains with a different composition will provide equal temperature conditions (the same for pressure). Estimated P-T conditions do not consequently depend on the different bulk rock compositions.

The P-T metamorphic conditions of the greenschist-facies event were estimated at 280 ± 30 °C, 7 ± 1 kbar. These conditions are in good agreement with zircon fission track ages (ZFTs) for the Pengguan massif, which have not been re-set since 200 Ma (Wang et al., 2012) and suggest that the massif remained below the ZFT closure temperature of ca. 270 °C (Tagami and Shimada, 1996) since the Triassic. The estimated temperature is also consistent with the T range below the plasticity field of feldspar (< 450 °C, Sibson, 2001) and close to the frictional-viscous transition of quartz (280 ± 30 °C, Stöckhert et al., 1999).

The P-T results indicate that the rocks of the Pengguan massif collected in the Lanjiaping and Yingxiu sectors were exhumed from 18 to 21 km depth (assuming a lithostatic pressure and a density for the crust of 2750 kg m^{-3}). The similarity in pressure (depth) estimates for both sectors suggests that spatial continuity of the exhumation depth recorded in the hanging wall of the Beichuan fault. The assumption of lithostatic pressure rather than local deviatoric pressure, is corroborated by the fact that samples distant of 70 km provide similar barometric results.

The low temperature recorded by our samples suggest a very low geothermal gradient of ca. 15 °C/km. Such a gradient is consistent with the thermal structure of stable continental regions (Kirby et al., 2002), is close to the geothermal gradient retrieved for the Yangtze craton from peridotites (Li et al., 2015 and references therein) and similar to modern gradients of 18–20 °C/km measured by the Wenchuan Fault drilling team in the Pengguan massif (Li et al., 2014a). This may explain why the greenschist-facies event does not develop pervasively in the

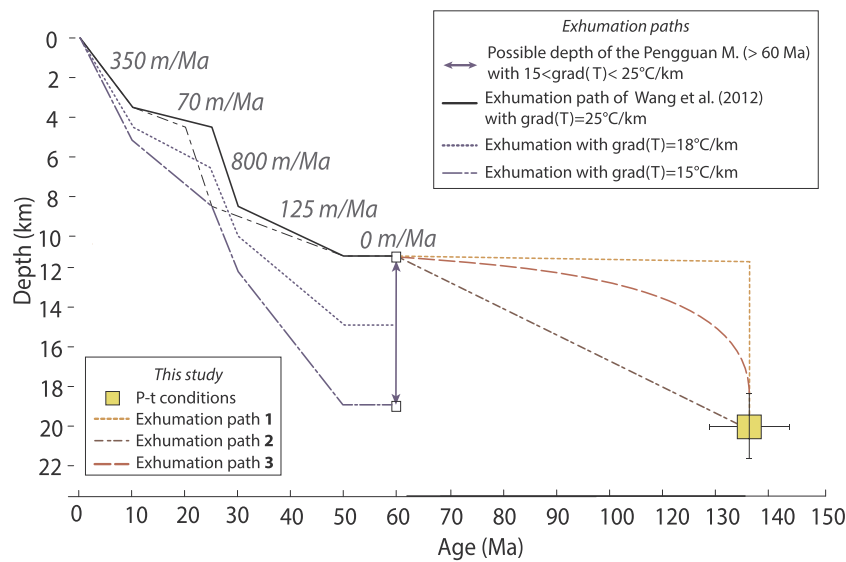


Fig. 9. Exhumation path of the Pengguan crystalline massif. Red: our results. Three possible exhumation paths relying the Lower Cretaceous cooling event to the Cenozoic one are proposed (1, 2, 3). Black: Wang et al. (2012) exhumation path. Numbers in m/Ma: exhumation rates. Yellow square: P-t conditions for the Pengguan massif at the lower Cretaceous. Blue arrow: range of possible depths for the Pengguan massif (at ca. 60 Ma) assuming a thermal gradient between 15 °C/km and 25 °C/km. Dashed and filled blue lines: exhumation paths recalculated from Wang et al. (2012) for a thermal gradient of 18 °C/km and 15 °C/km. (For interpretation of the references to colour in this figure legend, the reader is referred to the web version of this article.)

whole Pengguan massif but is only expressed in zones of strong deformation. At 20 km depth, with a cold geothermal gradient, the deformation can be greatly localized and brittle deformation can coexist with ductile deformation, as shown by our field observations. At this depth the rocks are close to the brittle-ductile transition zone.

6.3. Age of the greenschist metamorphism

The very small size of metamorphic K-white mica made it difficult to date the greenschist overprint affecting the Pengguan massif. Lower Cretaceous $^{40}\text{Ar}/^{39}\text{Ar}$ ages of 137 ± 3 Ma were obtained on M2-K-white micas of deformed granodiorite Y113-1c. Other Lower Cretaceous ages have been reported across the Longmen Shan, including 120–130 Ma white mica $^{40}\text{Ar}/^{39}\text{Ar}$ ages recorded in the hanging wall of the Wenchuan fault (Arne et al., 1997), and $^{40}\text{Ar}/^{39}\text{Ar}$ biotite ages of 120–123 Ma obtained in the Danba area (SW of the Longmen Shan; Xu et al., 2008).

The closure temperature of the Ar system in white micas (500–300 °C), still strongly debated, can depend on several parameters such as grain size, chemical composition and cooling rate (Villa, 1998). However, the estimated temperature for the metamorphic greenschist assemblage in our samples is below the minimum closure temperature of Ar system in white mica (Harrison et al., 2009; Warren et al., 2012) suggesting that the $^{40}\text{Ar}/^{39}\text{Ar}$ dates of these micas should be interpreted as crystallization ages. This is therefore also the age of the deformation affecting the samples from the Pengguan massif.

The Lower Cretaceous re-activation of the basement at temperature close to the ZFT closure temperature may have locally led to the partial annealing of ZFTs and could explain, for example, younger (110 Ma) ZFT ages obtained in the South-East of the Pengguan massif (Arne et al., 1997). Since the metamorphic record is restricted to areas of intense top to SE deformation, we propose that lower Cretaceous ages correspond to a thickening phase during which the Pengguan massif underwent a rapid pulse of exhumation, driven by (re)activation of the Triassic/Jurassic Beichuan fault. During this event the exhumation was only partial and the Pengguan massif did not reach the surface, as demonstrated by the lack of basement pebbles in the sediments of the foreland basin prior to Eocene time (Yong et al., 2003; Robert et al., 2010a).

6.4. Implications for the deep structure of the Beichuan fault

Presently, the Beichuan fault behaves as a thrust and dextral strike slip fault as shown by the 2008 Wenchuan earthquake (Fielding et al., 2013; de Michele et al., 2010a,b; Liu-Zeng et al., 2009). Our petrological observations underline the existence of a lower Cretaceous metamorphic event localized in the hanging wall of the Beichuan fault while no metamorphism was observed in the footwall of the fault. This evidence attests to a long term (hundreds to tens Ma) thrusting component of the fault that allowed the exhumation of the Pengguan crystalline massif along the Beichuan fault. The activation of the Beichuan fault may have caused significant uplift, which resulted in the localization of the erosion in the hanging wall of the fault. The Beichuan fault is consequently one of the major long-term structures of the Longmen Shan, as has already been suggested (Godard et al., 2009; Kirby et al., 2003).

Our P-T conditions indicate 20 ± 1 km of exhumation for the Pengguan massif since the Lower Cretaceous along the Beichuan fault. This implies that the Beichuan fault is rooted in the crust at a minimal depth of 20 km, in agreement with seismological studies imaging a basal detachment at 15–25 km depth, extending westward below the Songpan-Ganze block (Wang et al., 2009, 2013; Robert et al., 2010a; Liu et al., 2014; Qi et al., 2011; Shen et al., 2009; Jia et al., 2010; Zhao et al., 2012). This mid-crustal detachment could be a major and long-term structure of the Longmen Shan.

6.5. Implications on the exhumation history of the Pengguan massif since the lower Cretaceous

This study shows that during the lower Cretaceous, the Pengguan massif experienced a metamorphic event at conditions of 7 ± 1 kbar, 280 ± 30 °C, implying a geothermal gradient of ca. 15 °C/km at that time. Since the ZFT analyses record middle-upper Triassic ages (Wang et al., 2012) almost no significant temperature variations appear to have occurred in the Pengguan massif from the Triassic to the lower Cretaceous. The subsequent Cenozoic exhumation history of the massif is well-resolved by low-T thermochronology (Wang et al., 2012; Kirby et al., 2002; Godard et al., 2009). The onset of rapid cooling from ~200 °C has been proposed in the late Cenozoic, associated with 8–12 km of denudation, for a nominal geothermal gradient > 20 °C/

km (Kirby et al., 2002; Wang et al., 2012). Our thermobarometric results showing that the Pengguan massif was exhumed from ca. 20 km (~7 kbar) would therefore imply an important amount of exhumation prior to the Cenozoic phase. The exhumation could have occurred entirely during the lower Cretaceous (path 1 in Fig. 9) or at a slow and constant rate between the Cretaceous and the Cenozoic (path 2 of Fig. 9; Roger et al., 2011). However, in the first scenario, (U-Th)/He analyses on zircon should record lower Cretaceous ages instead of Cenozoic ones (ca. 45 Ma, Wang et al., 2012) and the second scenario would not be compatible with the pulse of fast exhumation required to explain the re-activation of Beichuan fault and the crystallization of the greenschist-facies assemblage. Moreover metamorphic minerals form the microstructures related to deformation. The intermediate path 3 in Fig. 9 is therefore, in our opinion, the most plausible exhumation path for the rocks of the Pengguan massif. Two pulses of rapid exhumation followed the Eocene cooling period: a first pulse took place at 30–25 Ma (at a rate of 800 m/Myr) (Wang et al., 2012) followed by a second period of fast cooling at ca. 10 Ma (Wang et al., 2012; Kirby et al., 2002; Godard et al., 2009) with exhumation rates of ca. 300–600 m/Myr (Godard et al., 2010).

It is crucial to note, however, that if the geothermal gradient was lower than 20°–30 °C/km (as shown in this study) at the time of the onset of exhumation, the depth of 8–12 km estimated with thermochronology for the Pengguan massif (Wang et al., 2012; Kirby et al., 2002) may have been largely underestimated (blue arrow and lines in Fig. 9). In this case it would be difficult to precisely define the amount of the pre-Cenozoic exhumation. Our study results therefore are the only independent depth information for the exhumation history. They indicate that a previously undocumented re-activation of the Pengguan massif (South China basement) precedes the Eocene-Miocene period of cooling and exhumation well documented in the central Longmen Shan by low-temperature thermochronology.

6.6. Implications on Mesozoic tectonic evolution of the Longmen Shan

Although several studies proposed a tectonic quiescence of the Longmen Shan during Middle Jurassic-Cretaceous times (Huang et al., 2003; Roger et al., 2011) the crystallization of a greenschist mineral assemblage indicates that the Beichuan fault was “re-activated” during lower Cretaceous. Indeed, Arne et al. (1997) interpreted their lower Cretaceous $^{40}\text{Ar}/^{39}\text{Ar}$ ages on white micas, obtained in the hanging wall of the Wenchuan fault, as a local reactivation of the fault zone at that time. Xu et al. (2008) associated lower Cretaceous $^{40}\text{Ar}/^{39}\text{Ar}$ biotite ages obtained in the mylonitic zone in Danba area to the formation of a detachment and consequent exhumation at the western margin of the Longmen Shan. Yan et al. (2011) also related the greenschist overprint observed in central LMS crystalline massifs to an extensional event occurred during the Early to Late Jurassic times. Lower Cretaceous $^{40}\text{Ar}/^{39}\text{Ar}$ ages (130–120 Ma) are documented further North, in the Tongbaishan-Hong’an-Dabieshan-Sulu massifs and are still associated with a fast cooling period followed by an Early Cretaceous extensional event (Lin et al., 2015). However no large-scale extensional structures have been observed in the field in the area of the Pengguan massif. On the contrary our results show that the Cretaceous greenschist metamorphic event is related to a top-to-SE deformation and thickening phase at the border of the Tibetan plateau. This is consistent with the ongoing development of a foreland basin during the lower Cretaceous in the western Sichuan basin due to the increase loading of the Longmen Shan and Qinling thrust belts (Li et al., 2003; Meng et al., 2005) (Fig. 10).

At a larger scale, the lower Cretaceous re-activation of the Longmen Shan in a compressive context could be due to: (i) the effects of the collision between the Lhasa and Qiantang blocks (Kapp et al., 2007) to the South West, followed by the eastward tectonic escape of the Songpan-Ganze block (ii) the Cretaceous re-activation of the Qinling-Dabie orogeny (Hu et al., 2006) (iii) the sinistral transpressional motion

of Longmen Shan and the clockwise rotation of the South China block based on the Northward migration of sedimentary depocenters in the Sichuan basin (Meng et al., 2005). A more extensive and detailed documentation of Cretaceous ages across the central Longmen Shan is however required in order to precisely discuss the tectonic evolution of the region throughout the whole Mesozoic.

No evidence of Triassic reactivation was founded in the Pengguan massif; we therefore infer that no significant thickening was recorded in the basement during the Triassic-lower Jurassic main compressional event. Sedimentary investigations, however, based on the migration of the carbonate ramp in the Sichuan Basin (Li et al., 2014b; Yong et al., 2003), suggest that an accretionary wedge was emplaced on the external zones of the Longmen Shan at ca. 230 Ma. This suggests a thin-skin deformation mechanism for the frontal part of the Longmen Shan accretionary wedge during the Triassic-lower Jurassic shortening (de Sigoyer et al., 2014). In this framework, the lower Cretaceous metamorphism recorded in the strongly deformed rocks of the Pengguan massif close to the Beichuan fault marks the propagation of the thick-skin deformation, involving basement slides, from the internal zones to the external zones of the Longmen Shan belt.

7. Conclusions

1. Field and petrographic observations show that the Pengguan crystalline massif underwent a greenschist facies metamorphic event associated with a brittle-ductile deformation in the hanging wall of the Beichuan fault.
2. High-resolution chemical analyses and thermobarometric calculations provide an estimate of the greenschist-facies P-T conditions at 280 ± 30 °C, 7 ± 1 kbar. The Pengguan massif was thus buried at ca. 20 km depth along a cold geothermal gradient of ca. 15 °C/km.
3. Metamorphic white mica $^{40}\text{Ar}/^{39}\text{Ar}$ ages show that the greenschist-facies metamorphism occurred at 137 ± 3 Ma, suggesting a “re-activation” of the Beichuan fault in the Lower Cretaceous.
4. The 20 ± 1 km of exhumation for the Pengguan massif since lower Cretaceous along the Beichuan fault constrains the minimal depth at which the fault is rooted in the crust. This depth estimate is in agreement with the depth of the basal detachment imaged by seismological studies below the Longmen Shan and the Songpan-Ganze block.
5. The metamorphic gap observed across the Beichuan fault underlines the importance of the long-term thrusting component of the fault.
6. The comparison between the available low-temperature thermochronological data for the Pengguan massif and our results suggest that the South China basement was partly exhumed along the Beichuan fault before the Eocene-Miocene exhumation phase (for a geothermal gradient of 30 °C/km). However, assuming a geothermal gradient of 15 °C/km, the uncertainty on the exhumation depths estimated with low-temperature thermochronology significantly increases, preventing the precise quantification of the pre-Cenozoic exhumation of the Pengguan massif.
7. No significant thickening of the basement (Pengguan massif) appears to have occurred during the upper Triassic - lower Jurassic compressional event, suggestive of a thin-skinned deformation in the external zones of the Longmen Shan. The re-activation of the Beichuan fault during the lower Cretaceous may therefore mark the onset of the thick-skinned deformation.

This study provides the first thermobarometric estimates for the Pengguan massif and an independent estimate for the total amount of exhumation recorded in the hanging wall of the Beichuan fault. It thus contributes to an improved model for the long-term thrusting process of the Longmen Shan tectonic system. Furthermore this work shows how petrology and thermobarometry in combination with published thermochronological data allow a refinement of the exhumation history of the crystalline massifs of the external zones of a thrust belt.

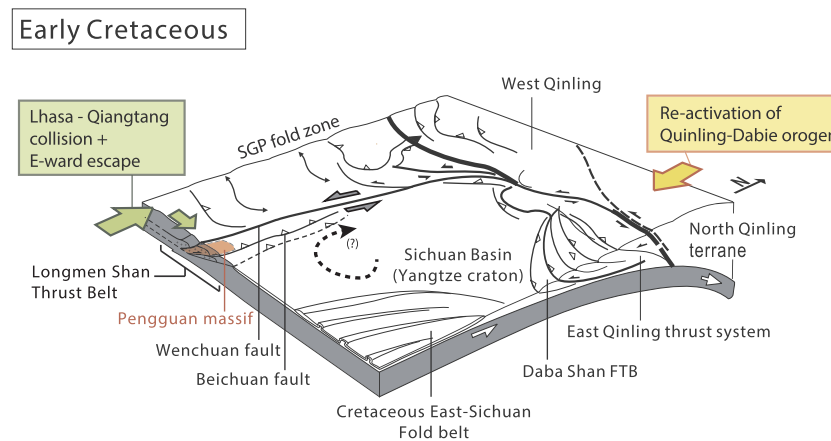


Fig. 10. Sketch showing the major tectonics implications at the Early Cretaceous based on the results of this study (modified from Meng et al., 2005). Green arrow: effects of the ongoing collision between Lhasa and Qiantang blocks. Yellow arrow: re-activation of the Qinling belt. The clockwise rotation of the Sichuan basin is from Meng et al. (2005). At Early Lower Cretaceous the Pengguan massif (red) did not outcrop at the surface; in agreement with the lack of basement pebbles in pre-Eocene sedimentary deposits of the frontal Longmen Shan (Yong et al., 2003; Robert et al., 2010a). (For interpretation of the references to colour in this figure legend, the reader is referred to the web version of this article.)

Acknowledgements

The project was made possible by the financial support of Agence Nationale de la Recherche (ANR) AA-PJCJC SIMI5-6 LONGRIBA, ANR-13-BS06-012-01 DSP-Tibet, the INSU-CNRS and LabEx “OSUG@2020” (ANR10 LABX56). We also thank professor Xu Xiwei (China Earthquake Administration), professor Li Yong (Chengdu University) and students from both universities, for their logistical support in the field and scientific discussions. The authors sincerely acknowledge E. Kirby and anonymous reviewers for their detailed, constructive and scientifically relevant reviews which strongly contributed to the improvement of the manuscript. We sincerely thank you Dr Clare J. Warren who strongly helped with editing the English. We also acknowledge Valérie Magnin, Valentina Batanova, Nataniel Findling for support with EPMA and SEM facilities.

Appendix A. Supplementary material

Supplementary data associated with this article can be found, in the online version, at <http://dx.doi.org/10.1016/j.jseas.2017.04.003>.

References

- Airaghi, L., Lanari, P., de Sigoyer, J., Guillot, S., 2017. Microstructural vs compositional preservation and pseudomorphic replacement of muscovite in deformed metapelites from the Longmen Shan (Sichuan, China). *Lithos* 282–283, 260–280. <http://dx.doi.org/10.1016/j.lithos.2017.03.013>.
- Arne, D., Worley, B., Wilson, C., Chen, S.F., Foster, D., Luo, Z.L., Liu, S.G., Dirks, P., 1997. Differential exhumation in response to episodic thrusting along the eastern margin of the Tibetan Plateau. *Tectonophysics* 280, 239–256.
- Billerot, A., 2011. De la marge Ouest du craton du Yangtze à la bordure Est du plateau Tibétain: Evolution géodynamique à partir de l'étude structurale, pétrologique, géochimique et géochronologique de roches magmatiques et métamorphiques. Ph.D. thesis Université Henri Poincaré, Nancy-University.
- Burchfiel, B., Chen, Z., Liu, Y., Royden, L., 1995. Tectonics of the Longmen Shan and adjacent regions, central China. *Intern. Geol. Rev.* 37, 661–735.
- Chen, S.F., Wilson, C., 1995. Emplacement of the Longmen Shan thrust-nappe Belt along the eastern margin of the Tibetan Plateau. *J. Struct. Geol.* 18, 413–430.
- de Michele, M., Raucoules, D., de Sigoyer, J., Pubellier, M., Chamot-Rooke, N., 2010a. Three-dimensional surface displacement of the 2008 May 12 Sichuan earthquake (China) derived from Synthetic Aperture Radar: evidence for rupture on a blind thrust. *Geophys. J. Int.* 1–7.
- de Michele, M., Raucoules, D., Lasserre, C., Pathier, E., Klinger, Y., Vand Der Woerd, J., de Sigoyer, J., Xu, X., 2010b. The Mw 7.9, 12 May 2008 Sichuan earthquake rupture measured by sub-pixel correlation of ALOS PALSAR amplitude images. *Earth Planets Space* 62, 875–879.
- de Sigoyer, J., Vanderhaeghe, O., Duchène, S., Billerot, A., 2014. Generation and emplacement of Triassic granitoids within the Sonpan Ganze accretionary orogenic wedge in a context of slab retreat accommodated by tear faulting, Eastern Tibetan plateau, China. *J. Asia Earth Sci.* 88, 192–216.
- Dirks, P.H.G.M., Wilson, C.J.L., Chen, S., Luo, Z.L., Liu, S., 1994. Tectonic evolution of the NE margin of the Tibetan Plateau; evidence from central Longmen Mountains, Sichuan Province, China. *J. Southeast Asia Earth Sci.* 9, 181–192.
- Dubacq, B., Vidal, O., De Andrade, V., 2010. Dehydraton of dioctahedral aluminous phyllosilicates: thermodynamic modelling and implications for thermobarometric estimates. *Contrib Mineral Petrol* 159, 159–174.
- Fielding, E., Sladen, A., Li, Z., Avouac, J.-P., Bürgmann, R., Ryder, I., 2013. Kinematic fault slip evolution source models of the 2008 M7.9 Wenchuan earthquake in China from SAR interferometry, GPs and teleseismic analysis and implications for Longmen Shan tectonics. *Geophys. J. Int.* 194, 1138–1166.
- Godard, V., Lav, J., Carcaillet, J., Cattin, R., Bourlis, D., Zhu, J., 2010. Spatial distribution of denudation in Eastern Tibet and regressive erosion of plateau margins. *Tectonophysics* 491, 253–274.
- Godard, V., Pik, R., Lav, J., Cattin, R., Tibari, B., de Sigoyer, J., Pubellier, M., Zhu, J., 2009. Late Cenozoic evolution of the central Longmen Shan, eastern Tibet: Insight from (U-Th)/He thermochronometry. *Tectonics* 28, TC5009.
- Harrison, T.M., Célérier, J., Aikman, A.B., Hermann, J., Heizler, M.T., 2009. Diffusion of ^{40}Ar in muscovite. *Geochim. Cosmochim. Acta* 73, 1039–1051.
- Hu, S., Raza, A., Min, K., Kohn, B.P., Reiners, P.W., Ketcham, R.A., Wang, J., Gleadow, A.J.W., 2006. Late Mesozoic and Cenozoic thermotectonic evolution along a transect from the north China craton through the Qinling orogeny into the Yangtze craton, Central China. *Tectonics* 25, TC6009.
- Huang, M., Maas, R., Buick, I.S., Williams, I.S., 2003. Crustal response to continental collision between the Tibet, Indian, South China and North China blocks: geochronological constrains from the Songpan-Ganze orogenic belt, western China. *J. Metamorph. Geol.* 21, 223–240.
- Hubbard, J., Shaw, J., 2009. Uplift of the Longmen Shan and Tibetan plateau, and the 2008 Wenchuan (M=7.9) earthquake. *Nature, Letters* 28, 1032–1047.
- Hubbard, J., Shaw, J., Klinger, Y., 2010. Structural Setting of the 2008 MW 7.9 Wenchuan, China, Earthquake. *Bull. Seismol. Soc. Am.* 100, 2713–2735.
- Jia, D., Guoqi, W., Chen, Z., Li, B., Zeng, Q., Yang, G., 2006. Longmen Shan fold-thrust belt and its relation to the western Sichuan Basin in central China: new insights from hydrocarbon exploration. *AAPG Bulletin* 90 (14), 1425–1447.
- Jia, D., Li, Y., Lin, A., Wang, M., Chen, W., Wu, X., Ren, Z., Zhao, Y., Luo, L., 2010. Structural model of 2008 Mw 7.9 Wenchuan earthquake in the rejuvenated Longmen Shan thrust belt, China. *Tectonophysics* 491, 174–184.
- Kapp, P., DeCelles, P.G., Gehrels, G.E., Heizler, M., Ding, L., 2007. Geological records of the Lhasa-Qiantang and Indo-Asia collisions in the Nima area of central Tibet. *GSA Bulletin* 119, 917–932.
- King, R.W., Shen, F., Burchfiel, B.C., Royden, L.H., Wang, E., Chen, Z., Liu, Y., Zhang, X.-Y., Zhao, J.-X., Li, Y., 1997. Geodetic measurement of crustal motion in southwest China. *Geology* 125, 179–182.
- Kirby, E., Reiners, P., Krol, M., Hodges, K., Whipple, K., Farley, K., Tang, W., Chen, Z., 2002. Late Cenozoic uplift and landscape evolution along the eastern margin of the Tibetan Plateau: inferences from $^{40}\text{Ar}/^{39}\text{Ar}$ and (U-Th)/He thermochronology. *Tectonics* 21 (1), 1001.
- Kirby, E., Whipple, K.X., Tang, W.Q., Chen, Z.L., 2003. Distribution of active rock uplift along the eastern margin of the Tibetan Plateau: inferences from bedrock channel longitudinal profiles. *J. Geophys. Res. – Solid Earth* 108, 2217.
- Kirby, E., Ouimet, W., 2011. Tectonic Geomorphology along the Eastern Margin of Tibet: Insights into the Pattern and Processes of Active Deformation Adjacent to the Sichuan Basin. Geological Society, London, Special Publications. V. 353, 165–188.
- Lanari, P., Guillot, S., Schwartz, S., Vidal, O., Tricart, P., Riel, N., Beysac, O., 2012. Diachronous evolution of the alpine continental subduction wedge: evidence from P-T estimates in the Briançonnais Zone houillère (France - Western Alps). *J. Geodyn.* 56–57, 39–54.
- Lanari, P., Vidal, O., De Andrade, V., Dubacq, B., Lewin, E., Grosch, E., Schwartz, S., 2014a. XMapTools: A MATLAB-based program for electron microprobe X-ray image processing and geothermobarometry. *Comput. Geosci.* 62, 227–240.
- Lanari, P., Wagner, T., Vidal, O., 2014b. A thermodynamic model for di-trioctahedral chlorite from experimental and natural data in the system $\text{MgO-FeO-Al}_2\text{O}_3\text{-SiO}_2\text{-H}_2\text{O}$.

- Applications to P-T sections and geothermometry. *Contrib. Miner. Petrol.* 167, 968.
- Li, H., Xu, Z., Niu, Y., Kong, G., Huang, Y., Wang, H., Si, J., Sun, Z., Pei, J., Gong, Z., Chevalier, M.L., 2014a. Structural and physical property characterization in the Wenchuan earthquake Fault Scientific Drilling project—hole 1 (WFSD-1). *Tectonophysics* 619, 86–100.
- Li, X., Zhu, P., Kusky, T.M., Gu, Y., Peng, S., Yuan, Y., Fu, J., 2015. Has the Yangtze craton lost its root? A comparison between the North China and Yangtze cratons. *Tectonophysics* 655, 1–14.
- Li, Y., Yan, Z., Liu, S., Li, H., Cao, J., Su, D., Dong, S., Sun, W., Yang, R., Yan, L., 2014b. Migration of the carbonate ramp and sponge buildup driven by the orogenic wedge advance in the early stage (Carnian) of the Longmen Shan foreland basin, China. *Tectonophysics* 619–620, 179–193.
- Lin, W., Ji, W., Faure, M., Wu, L., Li, Q., Shi, Y., Scharer, U., Wang, F., Wang, Q., 2015. Early Cretaceous extensional reworking of the triassic HP-UHP metamorphic orogen in Eastern China. *Tectonophysics* 662, 256–270.
- Liu, Q., van der Hilst, R., Yao, H., Chen, J., Guo, B., Qi, S., Wang, J., Huang, H., Li, S., 2014. Eastward expansion of the Tibetan Plateau by crustal flow and strain partitioning across faults. *Nat. Geosci.* 7, 361–365.
- Liu-Zeng, J., Zhang, Z., Wen, L., Tapponnier, P., Sun, J., Xing, X., Hu, G., Xu, Q., Zeng, L., Ding, L., Ji, C., Hudnut, K., van der Woerd, J., 2009. Co-seismic ruptures of the 12 May 2008, Ms 8.0 Wenchuan earthquake, Sichuan: east-west crustal shortening on oblique, parallel thrust along the eastern edge of Tibet. *Earth Planet. Sci. Lett.* 286, 355–370.
- Meng, Q.-R., Wang, E., Hu, J.-M., 2005. Mesozoic sedimentary evolution of the northwest Sichuan basin: implication for continued clockwise rotation of the South China block. *GSA Bulletin* 117, 396–410.
- Min, K., Mundil, R., Renne, P.R., Ludwig, K.R., 2000. A test for systematic errors in $^{40}\text{Ar}/^{39}\text{Ar}$ geochronology through comparison with U/Pb analysis of a 1.1-Ga rhyolite. *Geochim. Cosmochim. Acta* 1, 73–98.
- Parra, T., Vidal, O., Agard, P., 2002. A thermodynamic model for Fe-Mg dioctahedral K white micas using data from phase-equilibrium experiments and natural polytypic assemblages. *Contrib. Miner. Petrol.* 143 (6), 706–732.
- Qi, W., Xuejun, Q., Qigui, L., Freymueller, J., Shaomin, Y., Caijun, X., Yonglin, Y., Xinzhaoy, Y., Kai, T., Gang, C., 2011. Rupture of deep faults in the 2008 Wenchuan earthquake and uplift of the Longmen Shan. *Nat. Geosci.* 4, 634–640.
- Robert, A., Pubellier, M., de Sigoyer, J., Vergne, J., Lahfid, A., Cattin, R., Findling, N., Zhu, J., 2010a. Structural and thermal characters of the Longmen Shan (Sichuan, China). *Tectonophysics* 491, 165–173.
- Robert, A., Zhu, J., Vergne, J., Cattin, R., Chan, L., Wittlinger, G., Herquel, G., de Sigoyer, J., Pubellier, M., Zhu, L., 2010b. Crustal structures in the area of the 2008 Sichuan earthquake from seismologic and gravimetric data. *Tectonophysics* 491, 205–2010.
- Roger, F., Jolivet, M., Cattin, R., Malavieille, J., 2011. Mesozoic-Cenozoic tectonothermal evolution of the eastern part of the Tibetan Plateau (Songpan-Ganze, Longmen Shan area): insights from thermochronological data and simple thermal modelling. *Geol. Soc. London, Special Publ.* 353, 9–25.
- Roger, F., Jolivet, M., Malavieille, J., 2010. The tectonic evolution of the Songpan-Garze (North Tibet) and adjacent areas from Proterozoic to Present: a synthesis. *J. Asia Earth Sci.* 39, 254–269.
- Roger, F., Jolivet, M., Malavieille, J., 2008. Tectonic evolution of the Triassic fold belts of Tibet. *C. R. Geosci.* 340, 180–189.
- Shen, Z.-K., Lü, J., Wang, M., Bürgmann, R., 2005. Contemporary crustal deformation around the southeastern borderland of Tibetan plateau. *J. Phys. Res.* 110, B11409.
- Shen, Z.-K., Sun, J., Zhang, P., Wan, Y., Wang, M., Bürgmann, R., Zeng, Y., Gan, W., Liao, H., Wang, Q., 2009. Slip maxima at fault junction and rupturing of barriers during the 2008 Wenchuan earthquake. *Nat. Geosci.* 2, 718–724.
- Sibson, R.H., 2001. Seismogenic framework for hydrothermal transport and ore deposit. *Soc. Econ. Geol. Rev.* 14, 25–50.
- Steiger, R.H., Jäger, E., 1977. Subcommission on geochronology: convention on the use of decay constants in geo- and cosmochronology. *Earth Planet. Sci. Lett.* 36, 359–362.
- Stöckhert, B., Brix, M.R., Kleinschrodt, R., Hurford, A.J., Wirth, R., 1999. Thermochronometry and microstructures of quartz – a comparison with experimental flow laws and predictions on the temperature of the brittle-plastic transition. *J. Struct. Geol.* 21, 351–369.
- Tagami, T., Shimada, C., 1996. Natural long-term annealing of the fission-track system around a granitic pluton. *J. Geophys. Res.* 101, 8245–8255.
- Tan, X.-B., Lee, Y.-H., Chen, W.-Y., Cook, K.L., Xu, X.-W., 2014. Exhumation history and faulting activity of the southern segment of the Longmen Shan, eastern Tibet. *J. Asian Earth Sci.* 81, 91–104.
- Vidal, O., De Andrade, V., Lewin, E., Munoz, M., Parra, T., Pascarelli, S., 2006. P-T deformation-Fe³⁺/Fe²⁺ mapping at the thin section scale and comparison with XANES mapping. Application to a garnet-bearing metapelite from Sambagawa metamorphic belt (Japan). *J. Metamorph. Geol.* 24, 669–683.
- Villa, I.M., 1998. Isotopic closure. *Terra Nova* 10, 42–47.
- Vidal, O., Parra, T., Vieillard, P., 2005. Thermodynamic properties on the Tschermak solid solution in Fe-chlorite: application to natural examples and possible role of oxidation. *Am. Mineral.* 90, 347–358.
- Wang, E., Kirby, E., Furlong, K., van Soest, M., Xu, G., Shi, X., Kamp, P., Hodges, K., 2012. Two-phase growth of high topography in eastern Tibet during the Cenozoic. *Nature*. <http://dx.doi.org/10.1038/NGEO1538>.
- Wang, M., Jia, D., Shaw, J., Hubbard, J., Lin, A., Li, Y., Shen, L., 2013. Active fault-related folding beneath an Alluvial Terrace in the Southern Longmen Shan Range Front, Sichuan Basin, China: implications for seismic hazard. *Bull. Seismol. Soc. Am.* 103 (4), 2369–2385.
- Wang, Z., Fukao, Y., Pei, S., 2009. Structural control of rupturing of the Mw7.9 2008 Wenchuan earthquake, China. *Earth Planet. Sci. Lett.* 279, 131–138.
- Warren, C., Hanke, F., Kelley, S.P., 2012. When can muscovite $^{40}\text{Ar}/^{39}\text{Ar}$ dating constrain the timing of metamorphic exhumation? *Chem. Geol.* 291, 79–86.
- Whitney, D.L., Evans, B.W., 2010. Abbreviations for names of rock-forming minerals. *Am. Mineral.* 95, 185–187.
- Worley, B.A., Wilson, C.J.L., 1996. Deformation partitioning and foliation reactivation during transpressional orogenesis, an example from the Central Longmen Shan, China. *J. Struct. Geol.* 18, 395–411.
- Wu, M.-C., Liu, J., Cosgrove, J., Mason, P., Yan, H., Chang, W.-Y., 2014. Modelling of Yingxiu-Beichuan fault zone based on refined Insar data of 2008 Wenchuan earthquake. *Tectonophysics* 630, 193–207.
- Xu, Z., Ji, S., Li, H., Hou, L., Fu, X., Cai, Z., 2008. Uplift of the Longmen Shan range and the Wenchuan earthquake. *J. Int. Geosci. Episodes* 31, 291–301.
- Yan, D.-P., Zhou, M.-F., Li, S.-B., Wei, G.-Q., 2011. Structural and geochronological constrains on the Mesozoic-Cenozoic evolution of the Longmen Shan thrust belt, eastern Tibetan Plateau. *Tectonics* 30, TC6005.
- Yan, D.P., Zhou, M.F., Wei, G.Q., Gao, J.F., Liu, S.F., Xu, P., Shi, X.Y., 2008. The Pengguan tectonic dome of the Longmen Mountains, Sichuan Province: mesozoic denudation of a Neoproterozoic magmatic arc-basin system. *Sci. China Press* 51, 1545–1559.
- Yong, L., Allen, P.A., Densmore, A.L., Qiang, X., 2003. Evolution of the Longmen Shan Foreland Basin (Western Sichuan, China) during the Late Triassic Indosinian Orogeny. *Basin Res.* 15, 117–138.
- Yong, L., Rongjun, Z., Densmore, A., Wilson, C., Ellis, M., 2006. The Geology of the Eastern Margin of the Qinghai-Tibet Plateau. Geological Publishing House, Beijing 9.
- Zhang, H., Zhang, P.E., Yin, J., Lui, C., Yu, G., 2011. Along-strike topographic variation of the Longmen Shan and its significance for landscape evolution along the eastern Tibetan Plateau. *J. Asia Earth Sci.* 40 (4), 855–864.
- Zhang, Z., Wang, Y., Chen, Y., Houseman, G., Tian, Wang, E., Teng, J., 2009. Crustal structure across the Longmenshan fault belt from passive source seismic profiling. *Geophys. Res. Lett.* 292, L17310 (365 x).
- Zhang, Z., Yuan, X., Chen, Y., Tian, X., Kind, R., Li, X., Teng, J., 2010. Seismic signature of the collision between the East Tibetan escape flow and the Sichuan Basin. *Earth Planet. Sci. Lett.* 292, 254–264.
- Zhao, G., Unsworth, M., Zhan, Y., Wang, L., Chen, X., Jones, A., Tang, J., Xiao, Q., Wang, J., Cai, J., Li, T., Wang, Y., Zhang, J., 2012. Crustal structure and rheology of the Longmenshan and Wenchuan mw 7.9 earthquake epicentral area from magnetotelluric data. *Geology* 40 (12), 1139–1142.